Ga-Modified YAG:Pr^{3+} Dual-Mode Tunable Luminescence Thermometers

Paulina Bolek[1,*], Justyna Zeler[1,2], Carlos D.S. Brites[2], Joanna Trojan-Piegza[1], Luís D. Carlos[1,2,*], and Eugeniusz Zych[1,2]

*paulina.bolek@chem.uni.wroc.pl, *lcarlos@ua.pt

[1] Faculty of Chemistry, University of Wroclaw, 14. F. Joliot-Curie Street, 50-383 Wroclaw, Poland
[2] Phantom-g, CICECO-Aveiro Institute of Materials, Physics Department, University of Aveiro, 3810-193 Aveiro, Portugal

keywords: luminescence thermometry, dual-mode thermometer, bandgap engineering, YAG, Pr^{3+}

Abstract

The temperature determination using luminescent materials is nowadays considered the perspective remote technique for temperature gauging, despite the few examples reported so far combining wide operating temperature range with satisfying relative thermal sensitivity and temperature uncertainty values. In this paper, we study the $Y_3(Al,Ga)_5O_{12}$:0.1%Pr phosphors with controlled Ga:Al composition to deliberately affect their luminescent properties. We demonstrate that the energy barrier for thermal quenching of the 5d-4f luminescence can be effectively tailored, yielding the fine tune of the thermometric parameters of these phosphors. By exploiting time-resolved and time-integrated approaches we show that the thermometers can cover the 17–700 K temperature range with a maximum relative sensitivity up to 3.6 %·K^{-1} and a temperature uncertainty as lower as 0.02 K. For each sample, the temperature readout of the distinct thermometric parameters is compared illustrating that the performance of the thermometers should also consider the relative temperature error between the calculated and the measured temperatures, besides relative thermal sensitivity and temperature uncertainty.

Introduction

Luminescence thermometry is nowadays considered one of the most promising and perspective remote techniques of temperature measuring [1–5]. The requirements for luminescent thermometers are dependent on the final application. For example, for biological and medical purposes, a relative thermal sensitivity (S_r) and a temperature uncertainty (δT) [1,2,4] of the measurements within a rather narrow range around the physiological temperature are of greatest importance [6–11]. In space research, on the contrary, the high performance in the cryo-range is the priority [12,13]. Some other applications, such as catalysis, aerospace, surface temperature measurements, protection of structural materials, would benefit from luminescent thermometers able to measure temperature over a wide range, at least a few hundred degrees, and even above 1000 °C [3,14,15]. Such luminescence thermometers may not display very high relative thermal sensitivity and/or very low accuracy over their whole operating range [1,3]. At the present early stage of the luminescence thermometry development, a few hundred degrees of operating range is considered a very good result. Clearly, new ideas are necessary to bring significant progress or breakthroughs for producing luminescent thermometers for a wide temperature operating range.

Ratiometric, self-referencing luminescence thermometers based on a ratio of intensities of two emission bands (often termed luminescence/fluorescence intensity ratio, LIR, or FIR) are considered one of the most versatile approaches [1,16]. It allows fast reading, does not require frequent calibrations, and may benefit from adjustable excitation intensity. For such thermometers, at least two emission bands with different temperature dependencies of their intensities are required. Also, the temperature-dependence of the luminescence decay time can be useful for covering wide temperature ranges [3,16–18]. Till now, the performance of thermometers using this approach is mostly lower compared to LIR thermometers, but it is not a definitive rule [18]. Thus, both methods are valuable and worth further development. Presently the temperature-dependent decay time thermometry is exploited for high-temperature measuring, mostly above 300 K and it is claimed that this approach is not perspective for low-temperature luminescence thermometry [14,19]. However, the results presented in this publication show that there is no such limitation if the 5d $\rightarrow$4f luminescence kinetics is considered.

It was recently pointed out that Pr^{3+} may be useful to broaden the range of operating temperature and improve the performance of the thermometer in terms of thermal sensitivity and temperature uncertainty [20–22]. Namely, to take full advantage of this ion, it was indicated to use both its intra- (4f→4f) and inter-configurational (5d→4f) transitions [20–22]. This approach was firstly examined in $Sr_2(Ge,Si)O_4$:Pr and $Lu_2(Ge,Si)O_5$:Pr [20,21,23]. These thermometers operate in the 15-700 K range showing a relative thermal sensitivity as high as 9.2 $\%\cdot K^{-1}$. These encouraging results substantiate a further exploration of this approach to luminescence thermometry.

A common drawback shared by the $Sr_2(Ge,Si)O_4$:Pr and $Lu_2(Ge,Si)O_5$:Pr phosphors mentioned above is their inefficient excitation by the 4f→$5d_1$ transition around 245-255 nm using the most practical Ozone-free Xe lamp combined with a monochromator [21]. To overcome this difficulty, we exploit in this work the garnet hosts, known by their very high crystal field exerted on the activator. Consequently, dopants as Ce^{3+} or Pr^{3+} show their 4f→$5d_1$ absorptions at moderate energies (longer wavelengths) [24,25]. For the Pr^{3+} ion, this transition appears typically around 280 nm in garnets [24,26,27] and is easily accessed using the radiation from a commercial Xe lamp. Therefore, we study the whole $Y_3(Al,Ga)_5O_{12}$:Pr family of compositions (with different Ga:Al ratio) to explore the bandgap engineering effect and exploiting both the 5d→4f and 4f→4f emissions [28–32].

Several consequences for the electronic structure of $Y_3(Al,Ga)_5O_{12}$:Pr phosphors result from the replacement of Al by Ga, as schematically depicted in **Figure 1a**. The focus of our approach is tuning the performance of luminescence thermometers controlling the energy difference between the $5d_1$ level of Pr^{3+} and the bottom of the conduction band (CB) of the host (**Figure 1a**). This can be attained by adjusting the Al/Ga ratio, as the Ga addition reduces the bandgap. This occurs due to lowering the minimum of the CB. In parallel, the valence band (VB), as well as the $5d_1$ level of Pr^{3+}, moves to higher energies [24,28,32]. For the $Y_3Al_5O_{12}$ host, the bandgap is 7.5 eV, while for the $Y_3Ga_5O_{12}$ one it is only 6.5 eV [24,33]. Consequently, the $5d_1$ level and the bottom of CB get systematically closer with increasing Ga content. As

a consequence, the thermal quenching of the 5d→4f emission occurs at lower temperatures with the increase of Ga in the host. The detailed electronic levels structure for the activator is given in **Figure 1b**. Its main luminescent transitions, important for luminescence thermometry, are indicated with arrows. The red arrows in **Figure 1b** reflect the red part of the luminescence from the $^3P_0$ level which overlaps with the red emission from the $^1D_2$ level. This presents some important consequences in the applications of luminescence thermometry, as detailed in the next sections. Finally, the addition of Ga reduces the energy of the lattice phonons, an overlooked or ignored fact in the previous reports on bandgap engineering. Here we show that this impacts the non-radiative relaxation pathways between the various Pr^{3+} levels [24], a crucial point for the design of the luminescent thermometer. We show the influence of these effects and their interplay on the performance of the $Y_3(Al,Ga)_5O_{12}$:Pr thermometers.

In this paper, we show that bandgap engineering, adjusting the Ga:Al ratio in the $Y_3(Al,Ga)_5O_{12}$:Pr phosphors, allows tuning the range of temperatures within which the 5d→4f luminescence of Pr^{3+} ion is present and at which temperature it is quenched. This, in turn, makes possible a precise calibration of temperatures at which the thermometer shows the highest relative thermal sensitivity as well as its overall operating range. Since both 5d→4f luminescence intensity and its decay time present temperature dependence in very much the same range, a dual-mode thermometer may be constructed, and its operating range can be tuned from cryo-range up to 600 K. Recently, Dramicanin reported that the temperature-dependence of the decay time of the 4f→4f luminescence of trivalent lanthanide (Ln^{3+}) ions is suitable for thermometry at high temperatures [14,19]. In this paper, we will show that in the case of 5d→4f interconfigurational transitions the emission decay time may also be used for temperature sensing at low and moderate temperatures. Admirable accuracy, well below 0.05 K, even at high temperatures, is an additional important advantage of $Y_3(Al,Ga)_5O_{12}$:Pr luminescence thermometers. Thus, we demonstrate that these phosphors are dual-mode temperature sensors exploiting the temperature dependence of the 5d→4f luminescence in steady-state and time-resolved modes.

Experimental section

Materials preparation: Powders of $Y_3(Al,Ga)_5O_{12}$:0.1mol%Pr were prepared using flux-aided synthesis (Li_2SO_4, Alfa Aesar, 99.7%) and stoichiometric mixtures of Y_2O_3 (Stanford Materials, 5N), Al_2O_3 (Roth, 4N5), Ga_2O_3 (AbCr, 4N), and Pr_6O_{11} (Stanford Materials, 5N) oxides. All reagents were thoroughly mixed and ground with the flux using acetone as a wetting agent, placed in a covered corundum crucible and heated at 1300 ºC for 5 hours in the air. After cooling to room temperature, the products were recovered by washing with an excess of hot distilled water a few times. Finally, the powders were dried at 80 °C for 10 hours in a laboratory vacuum dryer. The following compositions were prepared and investigated: $Y_3Al_5O_{12}$:0.1mol%Pr, $Y_3(Al_4Ga_1)O_{12}$:0.1mol%Pr, $Y_3(Al_3Ga_2)O_{12}$:0.1mol%Pr, $Y_3(Al_{2.5}Ga_{2.5})O_{12}$:0.1mol%Pr, $Y_3(Al_2Ga_3)O_{12}$:0.1mol%Pr, $Y_3(Al_{1.5}Ga_{3.5})O_{12}$:0.1mol%Pr, $Y_3(Al_1Ga_4)O_{12}$:0.1mol%Pr, and $Y_3Ga_5O_{12}$:0.1mol%Pr. All powders were snow-white indicating that Pr^{4+} ions, giving broad-band charge-transfer absorption in the visible part of spectrum, were practically absent.

Structural and morphological analysis: Phase purity of all the materials was verified employing the X-ray powder diffraction (XRD) measurements in the range 2θ = 0-80º with the step 2θ = 0.01608º using a D8 Advance X-ray Diffractometer from Bruker. The Ni-filtered Cu $K_{\alpha 1}$ radiation (λ = 1.540596 Å) from a Cu X-ray tube was utilized. The microstructure of the powders was tested by scanning electron microscopy (SEM) with a Hitachi S-3400N electron microscope equipped with energy-dispersive X-ray spectroscopy (EDS) EDAX analyzer.

Photoluminescence: Photoluminescence excitation and photoluminescence spectra, as well as decay kinetic curves, were measured with an FLS 980 Spectrometer from Edinburgh Instruments Inc. equipped with a 450 W Xenon lamp for continuous and 60 W Xenon flash lamp for pulse excitation. The equipment was combined with a closed-cycle helium cryostat with a Cu holder for a sample mounting. The thermocouple type E (Nickel-Chromium/Constantan) placed close to the sample was used to measure the temperature.

The spectra were recorded in the 13–700 K temperature range with the 25 K step using Hamamatsu R928P high-gain photomultiplier thermoelectrically cooled to -20 °C with a Peltier module and operating in the range 200–870 nm. TMS302 X single grating excitation and emission monochromators of 30 cm focal lengths were utilized in the excitation and emission channels. The slits were 0.25 nm and the step 0.15 nm. Photoluminescence excitation spectra were corrected for the incident light intensity and photoluminescence spectra for the wavelength dependence of the spectral response of the recording channel. The time-resolved emission spectra and decay kinetic curves were taken upon the 60 W Xe pulse lamp excitation. The EPLED-280 (280 nm) pulse laser was used to excite the phosphors to measure the decay kinetic curves of the 5d→4f luminescence of Pr^{3+}. The emitted light was then recorded using an F-G05 low-noise photomultiplier featuring a Hamamatsu H5773-04 detector.

Infrared spectroscopy: Infrared (IR) spectra of the $Y_3(Al,Ga)_5O_{12}$:0.1%Pr powders were measured using a Bruker IFS66 spectrophotometer. Spectra were registered in the 50-4000 cm^{-1} range at 300 K using the classic nujol technique.

Thermometric Analysis: All photoluminescence spectra were converted from photon flux per constant wavelength interval function (as measured) into photon flux per energy interval according to the Jacobian transformation (relevant to ensure that the area underneath the spectrum is the same compared to integration in the wavelength scale) [34–37]. The integrated areas of the indicated transitions were calculated after the standard baseline subtraction [3]. Integrated intensities of selected luminescence bands (I_i) were calculated according to:

$$I_i = \int_{E_1}^{E_2} f\,(E,T)\,dE. \qquad \textbf{(1)}$$

The thermometric parameter, Δ, was defined as a ratio of integrated intensities of two specified transition bands (I_i and I_j, see Eq. (1)) as a function of temperature:

$$\Delta = \frac{I_i}{I_j}. \qquad \textbf{(2)}$$

The relative uncertainty in Δ was determined using [1]:

$$\frac{\delta\Delta}{\Delta} = \sqrt{\left(\frac{\delta I_1}{I_1}\right)^2 + \left(\frac{\delta I_2}{I_2}\right)^2} \qquad \textbf{(3)}$$

where $\delta I/I$ represents the relative uncertainty in the integrated area that is estimated using the signal-to-noise ratio of the emission spectra (dividing the readout fluctuations of the baseline by the maximum intensity value). Finally, empirical 2nd-degree polynomial functions were fitted to the experimental data to get the $\delta I/I$ temperature dependence.

The main parameters describing the thermometer performance are the relative thermal sensitivity (S_r) and the temperature uncertainty (δT) defined by [1,38,39]

$$S_r = \frac{1}{\Delta}\left|\frac{\partial \Delta}{\partial T}\right|, \quad \text{for intensity ratio} \qquad S_r = \frac{1}{\tau}\left|\frac{\partial \tau}{\partial T}\right|, \quad \text{for lifetime} \qquad \textbf{(4)}$$

$$\delta T = \frac{1}{S_r}\frac{\delta \Delta}{\Delta}, \quad \text{for intensity ratio} \qquad \delta T = \frac{1}{S_r}\frac{\delta \tau}{\tau}, \quad \text{for lifetime} \qquad \textbf{(5)}$$

where τ is the decay time of the 5d→4f luminescence and $\delta\tau/\tau$ its relative uncertainty. As a rule of thumb, the temperature operating range was defined considering that the difference between consecutive Δ or τ measurements in the acquisition of the respective calibration curve must surpass their corresponding uncertainties $\delta\Delta$ or $\delta\tau$ [40]. The thermometers are also out of their operating ranges if one value of Δ (or τ) corresponds to two (or more) different temperatures. To calculate $\delta\tau/\tau$ we fitted the experimental $\delta\tau/\tau_{max}$ values using polynomial functions (τ_{max} is the maximum value of the lifetime of each sample). The reproducibility was measured for each sample in 5 consecutive heating-cooling cycles recording and comparing the relative intensities of the luminescent bands of interest at 17 and 600 K.

Results and discussion

Effect of Ga:Al ratio on the structure and IR spectroscopy of $Y_3(Al,Ga)_5O_{12}$:Pr

The $Y_3Al_5O_{12}$ garnet crystallizes in the cubic structure, space group $Ia\bar{3}d$. The general formula of garnets is $A_3B_2C_3O_{12}$, where *A* represents a dodecahedral site with 8-fold coordination, *B* is an octahedral site showing 6-fold coordination, and *C* is a tetrahedral site of 4-fold coordination. In YAG, site *A* is occupied by Y^{3+} while *B* and *C* are occupied by Al^{3+} [41,42]. The ionic radii in the dodecahedral site for Y^{3+} and Pr^{3+} are 1.019 and 1.126 Å, respectively [43]. Al^{3+} and Ga^{3+} are much smaller ions and they fit the octahedral (0.535 and 0.62 Å) and tetrahedral (0.39 and 0.42 Å respectively) sites [40]. Consequently, the Pr^{3+} ion substitutes the Y^{3+} dodecahedral position due to the similarity of its radius to Y^{3+}. Hence, in general, Pr^{3+}

experiences one type of symmetry in the $Y_3(Al,Ga)_5O_{12}$ hosts. Substitution of Al^{3+} by larger Ga^{3+} necessarily enlarges the unit cell parameters and consequently elongates the bonds. Details of these changes readers may find in [44].

XRD patterns of all the investigated compositions are presented in **Figure S1a**. The measured diffractograms agree very well with the literature data (ICSD#16825 for $Y_3Al_5O_{12}$ and ICSD#14343 for $Y_3Ga_5O_{12}$) [45,46]. With the increase of the Ga content, the reflections shift towards smaller angles which corresponds to the increase of the unit cell as expected for the mentioned difference in the radii of Ga^{3+} and Al^{3+}. This effect is exposed in **Figure S1b** for the strongest line located at $2\theta \sim 33.3°$. Furthermore, the (Al,Ga) mixed compositions show a noticeable broadening of the diffraction lines resulting from the distortion of the structure caused by the discrepancy of the ionic radii of Al^{3+} and Ga^{3+} ions. This is also expected to exert some effects on the spectroscopy of the Pr^{3+} ions along the $Y_3(Al,Ga)_5O_{12}$:0.1mol%Pr series, as detailed next.

Figure S2 presents SEM images of all the investigated $Y_3(Al,Ga)_5O_{12}$ phosphors. The grains of the $Y_3(Al,Ga)_5O_{12}$ powders are mostly monocrystalline and form regular, well-shaped polyhedra. The average size of grains does not vary significantly. Most crystallites are ~1-2 μm in diameter but larger grains are also seen. Because the morphology of all powders is very similar it certainly does not account for any differentiations in the phosphors' luminescent properties.

Figure 2 presents IR spectra of all the $Y_3(Al,Ga)_5O_{12}$:0.1%Pr powders in the range of stretching vibrations of the AlO_4/AlO_6 and the GaO_4/GaO_6 moieties (500–900 cm^{-1}) [47,48]. These spectra expose that higher-frequency bands in the range 680–820 cm^{-1} (the grey region in **Figure 2**) are related to vibrations of the AlO_4/AlO_6 groups. The intensity of these bands decreases continuously with decreasing content of Al. The vibrations of the GaO_4/GaO_6 units which appear at around 570−720 cm^{-1} (the blue region in **Figure 2**) [47] are then growing in intensity and become the only vibrations visible in the $Y_3Ga_5O_{12}$ powder. A significant broadening of the observed features of the (Ga,Al) mixed materials is seen confirming the expected (and

observed in the XRD patterns in **Figure S1**) structural disturbance of the vibrating moieties in the mixed phosphors. Clearly, with the increasing Ga content in the host, the energy of the available phonons noticeably decreases. This is expected to affect the radiative and non-radiative relaxation of excited electron passageways and consequently the temperature dependence of the emission intensities of the various transitions of Pr^{3+}.

Photoluminescence spectroscopy at room temperature

Figure S3 presents the 300 K excitation spectra monitoring the luminescence of the $^1D_2 \rightarrow {}^3H_4$ transition, at 605 nm (**Figure S3a**), and the emission spectra **(Figure S3b)** excited into the maximum of the $4f \rightarrow 5d_1$ excitation band in the ultraviolet (UV) spectral range, for all the $Y_3(Al,Ga)_5O_{12}$ phosphors. The maximum of the $4f \rightarrow 5d_1$ excitation band is systematically shifted from about 290 nm in $Y_3Al_5O_{12}$:0.1%Pr to 275 nm in $Y_3Ga_5O_{12}$:0.1%Pr (see **Figure S3a**). This shift reflects the continuously smaller crystal field exerted by the surrounding ligands on the Pr^{3+}, with the increasing Ga content (due to the larger size of Ga^{3+} compared to Al^{3+} [47,49,50] causing elongation of the Pr^{3+}-O^{2-} distance). The intensities of the $4f \rightarrow 4f$ transitions relative to the $4f \rightarrow 5d$ one are more intense in the transitional $Y_3(Al,Ga)_5O_{12}$:0.1%Pr compositions, and not for purely stoichiometric $Y_3Al_5O_{12}$:0.1%Pr or $Y_3Ga_5O_{12}$:0.1%Pr. This may result from some inevitable distortion of the local symmetry of the Pr^{3+} emitting ion in the (Al,Ga) mixed hosts. Such a lowering of symmetry is in favor of higher transition rates of the intraconfigurational 4f-4f transition rates. As anticipated in the Introduction, the excitation was indeed efficiently executed with an Ozone-free Xe lamp. It directly impacts the thermometric performance by lowering the temperature uncertainty of these luminescence thermometers. This will be shown below in the Luminescence thermometry section.

Besides the broad UV band, the excitation spectra contain a set of narrow lines around 450–500 nm due to the $^3H_4 \rightarrow {}^3P_J$ transitions and similarly narrow lines around 590 nm (**Figure S3a**) resulting from the $^3H_4 \rightarrow {}^1D_2$ transition. The parity-allowed $5d \rightarrow 4f$ luminescence is fully quenched at 300 K in $Y_3Ga_5O_{12}$:0.1%Pr and $Y_3(Al_1Ga_4)O_{12}$:0.1%Pr phosphors, see **Figure S3b**. Clearly, in these two materials, the emitting $5d_1$ level

is either immersed within the host CB or close enough to it for the photoionization of the excited electron at 300 K. This accords with the scheme presented in **Figure 1a** and, obviously, precludes the 5d→4f luminescence from appearing. This accords with the conclusions drawn for similar compositions activated with Ce^{3+} [51].

The emission spectra at 300 K presented in **Figure S3b** demonstrate that the increasing content of Ga favors the bluish-green luminescence from the $^3P_0$ level around 485 nm compared to the red emission around 600–610 nm range. The latter, as will be shown below, is mostly composed of luminescence from the $^1D_2$ level (see **Figure 1b**). The dependence of the $^3P_0/^1D_2$ emission intensities ratio on Ga:Al ratio is anticipated to results from the lower energy phonons available for multiphonon relaxation when the Ga content increases (**Figure 2**). This observation reveals that Ga:Al ratio in the $Y_3(Al,Ga)_5O_{12}$:Pr garnets affects both the 5d→4f luminescence and also the 4f→4f radiative transitions.

According to the rule of thumb for Ln^{3+} ions, a co-called gap law for multiphonon non-radiative relaxation rate, k_{NR}, is expressed by:[35]

$$k_{NR} \sim e^{-\beta \frac{\Delta E}{\hbar \omega_{max}}}, \qquad \textbf{(6)}$$

where $\frac{\Delta E}{\hbar \omega_{max}}$ is called the reduced energy gap and defines the number of phonons of maximum frequency (ω_{max}) available in the system required to bridge two consecutive electronic levels (and allow for non-radiative relaxation between them) and β is frequency constant weakly dependent on temperature [35]. When the needed number of phonons of maximum available frequency exceeds ~5–6, the radiative relaxation of the higher level dominates (*i.e.*, the rate of the non-radiative process is very low), while for

lower numbers the non-radiative (multiphonon) relaxation becomes significant resulting finally in a total luminescence quenching of the higher-energy level [35].

Because the energy gap between the $^3P_0$ and $^1D_2$ levels is about 4000 cm^{-1} [52], the vibrations of AlO_4 and AlO_6 groups (~800 cm^{-1}) may quite effectively drain the electrons from the $^3P_0$ to $^1D_2$ level. However, the effectiveness of the GaO_4 and GaO_6 vibrations (~700 cm^{-1}) for such a process has to be noticeably lower and this is exactly what we note in the luminescence spectra presented in **Figure S3**. Altogether, we may summarize that bandgap engineering significantly affects the energy relaxation from $5d_1$ level to all the lower-lying 4f levels of the Pr^{3+}. Consequently, the intensity of the 5d→4f band correlated with the 4f→4f ones strongly depends on the Ga:Al ratio. Moreover, upon **Eq. 6**, the decrease of the energy of host lattice phonons with the increase of Ga reduces the efficiency of the non-radiative thermalization of electrons from the $^3P_0$ to $^1D_2$ level. These two different effects, bandgap modification as well as decrease of energy of host lattice phonons, are both caused by the replacement of Al with Ga. This has to impact the performance of the luminescence thermometers.

Temperature-dependent emission spectra

Figure 3 presents the emission spectra in the 17–700 K range under 4f→$5d_1$ (in the UV spectral range, **Figure S3a**) excitation. A broad emission band peaking at 310 nm dominates the spectra at low temperatures for all investigated samples except the $Y_3(Al_1Ga_4)O_{12}$:0.1%Pr and $Y_3Ga_5O_{12}$: 0.1%Pr in which the 5d→4f luminescence is not registered even at 17 K. It was reported that a trace of this emission could be recorded in $Y_3Ga_5O_{12}$:Pr at 10 K [24]. This implies that the $5d_1$ level almost coincides with the bottom of the host CB, as predicted by the Dorenbos model and presented in **Figure 1a**.

Upon temperature increase, the 5d→4f luminescence disappears in all compositions although at different temperatures, with the concurrent increase of the emission in the bluish-green ($^3P_0$→$^3H_{4,5}$) and the red part of the spectrum ($^3P_0$→$^3H_6$ and $^1D_2$→$^3H_{4,5}$) observed up to 700 K, see **Figure 3**. Hence, upon heating, at

least part of the energy from the $5d_1$ level is transferred to the $^3P_0$ and/or $^1D_2$ states. Though this is true for all compositions, it is more evident for the Ga-free sample. In it, the energetic separation between the CB and the $5d_1$ level is maximized (**Figure 1a**), repressing the thermally-induced photoionization of the $5d_1$ excited state and favoring the $5d_1$-to-^3P_J crossover flow of the excited electron [24].

We rationalize the observed temperature-induced changes in emission spectra taking into account that in the visible range the spectra consist of a series of overlapped narrow lines. The $^3P_0 \rightarrow {}^3H_4$ transition in the 450-500 nm spectral range and the 590-650 nm part, which comprises superimposed transitions from $^1D_2$, as well as $^3P_0$ levels, are observed [20–22,53,54]. The assignment of the two contributions in the red is crucial for determining refined thermometric parameters [1–3,16]. Therefore, we use time-resolved emission spectroscopy (TRES) to effectively resolve them.

Since the transition from the $^3P_0$ level is spin-allowed, its decay time is much faster than the spin- and parity-forbidden transitions responsible for the emission lines originated from the $^1D_2$ level. **Figure S4** presents the bidimensional TRES maps for all the investigated phosphors. Note that the measurements were performed at different temperatures. At higher temperatures, a significant broadening of the emission lines is seen, as expected. On top of them, the emission spectra registered after two different delay times (so-called fast and slow components) are presented. Most of the slower $^1D_2$ luminescence is located in the ~605−610 nm range for all the samples. Therefore, to determine the integrated intensity of the $^1D_2 \rightarrow {}^4H_{4,5}$ transition, we set these integration limits.

Temperature-dependent lifetimes

Figure S5 presents decay curves of the 5d→4f luminescence for all the Pr^{3+}-doped materials studied at 17 K and 300 K. The experimental decay curves were fitted using:

$$I(t) = A_0 + \sum_{i=1}^{N} A_i \times \exp\left(-\frac{t}{\tau_i}\right), \quad \textbf{(7)}$$

where *I(t)* represents intensity after time *t*, A_i is a fitting parameter (accounts for the weight of the i-th component in the fit), τ_i is the decay time of the i-th component, and A_0 is a background intensity. For all decay traces, two components were used (N=2) to get satisfying fits. However, the deviation from the single-exponential dependence (N=1) was only minor in most cases. The low-temperature decay time of the 5d→4f luminescence in $Y_3Al_5O_{12}$:Pr sample is τ = 21.0±0.5 ns, a value that perfectly meets the ones reported in the literature (18-22 ns) for single crystals [55,56], which may be taken as proof of the high quality of the powder phosphors. The decays at 300 K, **Figure S5b**, for the Ga-containing compositions are characterized by shorter decay times than those registered at 17 K.

The thermal quenching of the 5d→4f luminescence (**Figure 3**) occurs either through cross-relaxation or photoionization processes depending on the Ga:Al ratio that determines the energy difference between the $5d_1$ level, and the minimum of the CB (**Figure 1a**) [24]. To determine the energy barrier for the mentioned quenching processes, decay traces of the 5d→4f emission were measured as a function of the temperature (**Figure 4a-g)**. The results show that the decay time recorded at the lowest temperature decreases with increasing Ga:Al ratio. Whereas for the $Y_3Al_5O_{12}$:0.1%Pr sample it is 21.0±0.5 ns, for the $Y_3(Al_1Ga_4)O_{12}$:0.1%Pr it is only 15.5±0.5 ns. This trend accords with **Eq. (8)**, which describes the dependence of the radiative decay time of an electric-dipole transition using parameters related both to the host lattice and to the luminescence center [57]:

$$\tau = 1.5 \times 10^{-5} \frac{9\lambda^2}{fn(n^2+2)^2}. \quad \textbf{(8)}$$

In **Eq. (8)**, f is the oscillator strength of the transition, λ stands for the emission wavelength in nanometers, and n is the material refractive index. In the investigated garnets the 5d→4f emission position does not move much so, λ can have only a limited effect, if any, on τ. This infers that the observed increase in the transition rate is mostly due to the powerful $\tau^{-1} \sim n^3$ dependence.

With an increasing Ga content, the quenching temperature ($T_{50\%}$, the temperature at which the decay time drops by a factor of 2 compared to its low-temperature value) of the 5d→4f emission first increases from 350 K in $Y_3Al_5O_{12}$:0.1%Pr to 420 K in $Y_3(Al_{2.5}Ga_{2.5})O_{12}$:0.1%Pr. For yet higher Ga concentrations a fast drop of $T_{50\%}$ takes place and in $Y_3(Al_1Ga_4)O_{12}$:0.1%Pr $T_{50\%}$ = 160 K.

The activation energies, ΔE_{ai}, of the 5d→4f emission quenching was calculated considering a single- (i=1) or a double-barrier (i=2) model:[54,58]

$$\frac{1}{\tau} = \frac{1}{\tau_0} + \sum_{i=1}^{2} B_i \times \exp\left(-\frac{\Delta E_{ai}}{k_B T}\right), \qquad \textbf{(9)}$$

where τ is the measured decay time at temperature T, τ_0 is the radiative decay time (assumed to be equal to the low-temperature experimental value), B_i are fitted pre-exponential factors, and k_B stands for the Boltzmann constant. Except for $Y_3(Al_1Ga_4)O_{12}$:0.1%Pr where a double-barrier model is used to calculate the activation energies ΔE_{a1} and ΔE_{a2}, the 5d→4f emission quenching in the remaining samples was described by a single-barrier model. **Figure 4a-g** presents the results of the fits using **Eq. (9)** (see also **Table S1**), and **Figure 4h** depicts graphically the changes on ΔE_{a1} for the different samples: from $Y_3Al_5O_{12}$:0.1%Pr to $Y_3(Al_{2.5}Ga_{2.5})O_{12}$:0.1%Pr ΔE_{a1} increases from 0.17±0.01 to 0.37±0.02 eV, decreasing quickly for the Ga-rich compositions reaching 0.070±0.004 eV for the $Y_3(Al_1Ga_4)O_{12}$:0.1%Pr phosphor.

These data will appear very useful while performing the calculations of the intensity-based thermometric parameters of these garnets. The results are in good agreement with the data presented by Ueda *et al.* in [24]. These authors found that in the Al-rich phosphors this is a thermally-activated cross-over mechanism that stands behind the 5d→4f luminescence quenching. On the contrary, in the Ga-rich materials the quenching results from thermally-induced photoionization of the 5d emitting level. It proves that our original preparation method did not affect this property to any significant degree.

The Ga content also affects the decay times of intra-configurational luminescence of the investigated phosphors. Analysis of this effect allows for a better understanding of the spectroscopy of Pr^{3+} in these hosts. The temperature dependence of the $^3P_0 \rightarrow {}^3H_4$ and $^1D_2 \rightarrow {}^3H_4$ luminescence decays are presented in **Figures S5c,d** and **Figures S5e,f**, respectively at 17 (**S5c,e**) and 300 K (**S5d,f**). The decay time of the $^3P_0$ bluish-green luminescence increases with the increasing content of Ga at both temperatures. In the Ga-free $Y_3Al_5O_{12}$:Pr the $^3P_0$ luminescence decay time is 14.0±0.1 μs both at 17 and 300 K. Yet, in the $Y_3(Al_1Ga_4)O_{12}$:Pr and the Al-free $Y_3Ga_5O_{12}$:Pr it approaches 22-24 μs, a 50 % increase. On the contrary, the decay time of the red luminescence resulting from the $^1D_2 \rightarrow {}^3H_4$ electronic transition changes only slightly (<5%) within the whole series of the $Y_3(Al,Ga)_5O_{12}$:Pr phosphors. At 17 K it reaches ~245-247 μs and at 300 K it is 210 μs in $Y_3Al_5O_{12}$:Pr and 215 μs in $Y_3Ga_5O_{12}$:Pr. Hence, the $^1D_2 \rightarrow {}^3H_J$ luminescence kinetics is much less affected by the Ga:Al ratio than the $^3P_0 \rightarrow {}^3H_J$ one.

These results are understandable considering the **Eqs. (6)** and **(8)** and the IR spectra presented in **Figure 2**. In the Ga-rich phosphors, the electron at the $^3P_0$ level is less prone to relax non-radiatively to the next lower-lying $^1D_2$ than in the Al-rich garnets because the former hosts offer less-energetic phonons than the latter one. Yet, one should be aware that the physics behind the experimentally observed spectroscopic properties of the $Y_3(Al,Ga)_5O_{12}$:Pr garnets is more complex. The changes of the Ga:Al ratio in the hosts affect at least their three important attributes, all pertinent to the activator luminescence properties: (i) refractive index, (ii) the host bandgap, and (iii) phonon energies of the host. The resulting properties observed experimentally

come from the interplay between them [35,57]. Analyzing the experimental results and considering just one of them may be easily misleading.

Luminescence thermometry

Luminescence intensities ratio

The temperature-induced change on the emission spectra of the Pr^{3+}-doped phosphors (**Figure 3**) motivated the application of the compounds for luminescent thermometry through the following thermometric parameters:

$$\Delta_1 = \frac{I_{df}}{I_{1D2}} \qquad \Delta_2 = \frac{I_{3P0}}{I_{1D2}} \qquad \Delta_3 = \frac{I_{df}}{I_{3P0}}, \qquad \textbf{(10)}$$

where I_{df}, I_{3P0}, and I_{1D2} corresponds to the integrated areas of the 5d→4f, $^3P_0 \rightarrow {}^3H_4$, and $^1D_2 \rightarrow {}^3H_4$ transitions, respectively. The integration ranges are shown in **Figure S6**, for the illustrative example of $Y_3Al_5O_{12}$:0.1%Pr. As the temperature dependence of I_{df} is much higher than those of I_{3P0} and I_{1D2} (**Figure S7**), we consider that the temperature dependences of Δ_1 and Δ_3 are determined essentially by the thermal quenching of the 5d→4f transition. Thus, and considering the S-shaped decrease on I_{df}, we rationalize the temperature dependences of Δ_1 and Δ_3 using the Mott-Seitz model with $N = 2$ or $N = 3$ non-radiative channels [59,60]:

$$\Delta_{1,3} \approx \frac{\Delta_0}{1 + \sum_{i=1}^{N} \alpha_i \exp\left(\frac{-E_{ai}}{k_B T}\right)}, \qquad \textbf{(11)}$$

where Δ_0 is the Δ parameter at the limit $T \rightarrow 0$ K, $\alpha_i = W_{0i}/W_{Ri}$ is the ratio of the nonradiative (W_{0i} at T→0 K) and radiative (W_{Ri}) rates and E_{ai}, is the energy barrier value for the non-radiative relaxations. The temperature dependence of Δ_1 is presented in **Figure 5** (fitted values in **Table S1)**, while **Figure S9a** (and **Table S3**) show the results for Δ_3. We recall that **Eq. (11)** encompasses the same fundamental principles of the single barrier model used for rationalizing the temperature dependence of the lifetime, although both Δ_1 and Δ_3 follow a double-S or for some samples a triple-S shaped dependence. Furthermore, we note that Δ_3 can be only calibrated through **Eq. (11)** because we are assuming that the rate of the thermal quenching of the 5d→4f luminescence is much higher than the $^3P_0$-to-$^1D_2$ temperature-dependent multiphonon relaxation rate. For Δ_1, however, an effective Mott-Seitz dependence is expected as the $^1D_2$ level is not prone to non-radiative quenching in the temperature range studied.

The resulting values of E_{a1}-E_{a3} are collected in **Tables S1 and S3** together with the energy barrier of the 5d→4f luminescence quenching found from decay kinetics (**Figure 4**). It is noteworthy that for each of the investigated phosphors the E_{a1} value of the Mott-Seitz model (**Eq. (11)**) agrees well with the energy barrier of the 5d→4f inter-configurational emission thermal quenching derived from its decay kinetics (**Figure S8**). This is an expected result and attests the applicability of the Mott-Seitz model for the systems studied here. The presence of the much smaller activation energies (E_{a2} and, in two cases, E_{a3}) has to result from yet another process, ineffective and presently not clearly defined. As discussed above, the complexity of the host-dopant interaction in these garnets, as well as the interaction of the emitting levels with a (nearby located) defect can play important roles in the generation of such tiny deviation. These garnets are known for the incorporation of various defects affecting their luminescence properties [31,61–63]. As seen in **Figure S5**, some decay curves show an afterglow component (a tail after the main, basically single exponential, part). This infers that defects interacting with the Pr^{3+} emitting ions are plausible entities affecting the relaxation processes.

The temperature dependence of the relative thermal sensitivity and temperature uncertainty for Δ_1 are presented in **Figure 6a,b** (the corresponding values for Δ_3 are presented in **Figures S9b,c**). The maximum value of the S_r parameter (hereafter denoted S_m [1]) related to Δ_1 varies in the 2.3–3.6 %·K^{-1} range. There is a trend observed in the change of the temperature (T_m) at which S_m occurs with increasing the Ga:Al ratio. For the lower Ga content, T_m grows becoming pretty similar for the intermediate compositions: $Y_3(Al_{2.5}Ga_{2.5})O_{12}$:0.1%Pr and $Y_3(Al_2Ga_3)O_{12}$:0.1%Pr. For yet higher Ga content T_m value decreases quickly reaching 60 K for $Y_3(Al_1Ga_4)O_{12}$:0.1%Pr. All the determined parameters of the thermometers are gathered and listed in **Table 1**. The highest S_m is reached by three phosphors: $Y_3(Al_{2.5}Ga_{2.5})O_{12}$:0.1%Pr shows S_m = 3.1 %·K^{-1} at 340 K, $Y_3(Al_{1.5}Ga_{3.5})O_{12}$:0.1%Pr with S_m = 3.6 %·K^{-1} at 237 K and $Y_3(Al_1Ga_4)O_{12}$:0.1%Pr attains a similar value of S_m = 3.6 %·K^{-1} at 60 K. Without doubts, the impact of the Ga content on the relative sensitivity and temperature of its maximal value is meaningful. Consequently, by bandgap engineering, fine-tuning of the $Y_3(Al,Ga)_5O_{12}$:Pr thermometers performance can be effectively executed, and their highest sensitivity adjusted to a specified range of temperatures.

The temperature dependence of the δT (related to the Δ_1, **Eq. (5)**) is presented in **Figure 6b** for all investigated garnets. In general, the values of δT are very low (except for very low temperatures) for $Y_3Al_5O_{12}$:0.1%Pr and $Y_3(Al_4Ga_1)O_{12}$:0.1%Pr, which results from very small intensities of their $^1D_2$ luminescence at such conditions. Nevertheless, practically over the whole operating ranges, the values of δT are well below 0.1 K, mostly even <0.05 K. This is a very good result, partially being the consequence of an efficient excitation of the garnet phosphors around 275–290 nm, which reduces the noise level. While the S_r values are similar for both Δ_1 and Δ_3 (**Figure 6a** and **Figure S9b**, respectively), the overall temperature uncertainty is lower for the latter, especially for $Y_3(Al_{1.5}Ga_{3.5})O_{12}$:0.1%Pr and $Y_3(Al_2Ga_3)O_{12}$:0.1%Pr (**Figure 6b** and **Figure S9c**). This is expected because the intensity of the $^3P_0$-based emission is usually higher than that from the $^1D_2$ level. Thus, despite Δ_3 is not an independent thermometric parameter ($\Delta_3=\Delta_1/\Delta_2$) it is extremely useful due to its lower temperature uncertainty.

Figure S10 presents the temperature-dependence of the Δ_2 thermometric parameter (**Eq. (12)**), corresponding S_r (**Figure S10b**), and δT (**Figure S10c**). As Δ_2 is defined as a ratio of intensities ascribed to intra-4f transitions, there is no obvious model to rationalize the temperature dependence. Indeed, the complete rationalization of the observed temperature dependence for the 4f→4f transitions requires the establishment and solving of the rate equations that describe this system, as done previously by Suta & Meijerink [37] and Geitenbeek *et al*. [64]. However, because the purpose here is merely the comparison between the thermal performance of the three thermometric parameters, that detailed analysis is out of the scope of the present work and, instead, we adopt an empirical curve to fit the Δ_2 data points. For this purpose, we used a second-degree polynomial function:[1]

$$\Delta_2 = C_1 + C_2 T + C_3 T^2, \qquad \textbf{(12)}$$

where C_1, C_2, and C_3 are fitting constants. For $Y_3(Al_3Ga_2)O_{12}$:0.1%Pr and $Y_3(Al_2Ga_3)O_{12}$:0.1%Pr, the $\Delta_2(T)$ dependence could not be well fitted using Eq. (12). Therefore, we separately analyze the data points into the ranges for which this is possible to implement (a similar approach was applied in reference [20]). All the fitting results are compiled in **Figure S10 and Table S2**.

For all the investigated $Y_3(Al,Ga)_5O_{12}$:0.1%Pr phosphors, the S_m and T_m values change with Ga concentration, see **Table 1**. The S_m values based on the Δ_2 are smaller compared to the just discussed results related to the Δ_1. Considering just the Δ_2, three phosphors present a notorious performance. In $Y_3Al_5O_{12}$:0.1%Pr, S_m = 2.5 %·K^{-1} at 600 K, in $Y_3(Al_2Ga_3)O_{12}$:0.1%Pr S_m = 1.0 %·K^{-1} at 100 K and in $Y_3(Al_{1.5}Ga_{3.5})O_{12}$:0.1%Pr S_m = 1.0 %·K^{-1} at 480 K. The temperature uncertainty related to Δ_2 does not exceed 1 K at low temperatures and for some compositions is lower than 0.2–0.3 K over wide ranges of

temperatures. Obviously, in the case of $Y_3Ga_5O_{12}$:0.1%Pr, the measurements are possible exclusively using Δ_2 as there is no 5d→4f luminescence in this phosphor.

We call attention to the illustrative example of $Y_3(Al_2Ga_3)O_{12}$:0.1%Pr (**Figure S10a**) for the definition of the temperature operating range when more than one calibration curve needs to be used for describing the temperature dependence of a thermometric parameter. In this sample, we need two curves for modeling $\Delta_2(T)$ because we can find two temperatures ascribed to the same Δ_2 value, meaning that a single Δ_2 value can be ambiguous for determining the temperature. As a consequence, one of the two calibrating ranges must be chosen to operate the thermometer. The temperature range in which the material is operating can be disambiguated by scanning two temperatures, as for each of the operating ranges Δ_2 is either continuously growing or continuously decreasing.

Decay time

It was presented in **Figure 4a-g** that the decay time of the 5d→4f luminescence shows strong temperature-dependence. We found these changes useful for temperature measuring.

Figure 7 depicts the temperature dependence of the relative sensitivity, S_r, and temperature uncertainty, δT, calculated using this approach, see **Eqs. (4)** and **(5)**. Depending on the composition, the S_m varies in the 0.7–1.5 %·K^{-1} range. The temperature of S_m (at T_m) shows a characteristic trend. It grows from 378 K in $Y_3Al_5O_{12}$:0.1%Pr to 480 K in $Y_3(Al_{2.5}Ga_{2.5})O_{12}$:0.1%Pr and for yet higher Ga contents, it quickly decreases reaching 184 K in $Y_3(Al_1Ga_4)O_{12}$:0.1%Pr. Two garnets present supreme performance considering the relative sensitivity based on the 5d→4f luminescence decay time. In $Y_3(Al_{2.5}Ga_{2.5})O_{12}$:0.1%Pr, S_m = 1.5%·K^{-1} at 480 K, and in $Y_3(Al_1Ga_4)O_{12}$:0.1%Pr S_m = 1.4%·K^{-1} at 184 K. Moreover, a broad operating range of $Y_3(Al_1Ga_4)O_{12}$:0.1%Pr is its additional advantage when the 5d→4f luminescence decay time is used.

The general observation is that the decay time of the 5d→4f luminescence allows measuring the temperature over quite broad ranges (changing characteristically with composition) and with very low uncertainty δT<0.02 K, see **Figure 7b**. This is an immensely low value, specifically at temperatures as high as 500–600 K.

The relative error of the different thermometric parameters

To represent the relative temperature error between the calculated and the measured temperatures we use violin plots (**Figure 8**). They compare the temperature readout of the distinct thermometric parameters (Δ_{1-3} and τ). Firstly, we converted each recorded thermometric parameter to the *calculated* temperature T_c using the corresponding calibration curve. This value was then compared with the temperature T_t *measured* by the thermocouple close to the sample. For each material, the absolute relative error was determined by $|T_c-T_t|/T_t$ for all the data points within the operating range of the thermometer. The resulting violin plots are modified boxplot graphical representations of data that include the probability density as the violin. This enables the visual evaluation of the distributions attained for distinct methods within the same sample.

The violin plots do not reflect the dependence of the thermometric performance on the Ga content (listed in **Table 1**), but, instead, provide a graphical picture of the deviations of the thermometric readout relative to the corresponding calibration curve in the entire operating range. Thermometers with better performance correspond to distributions with the higher width at a lower relative error value reveals that in different samples the temperature relative error is minimized for distinct parameters, within the operating range of the thermometers. While for $Y_3(Al_4Ga_1)O_{12}$:0.1%Pr, for instance, the decay time analysis produces the best results, for $Y_3(Al_1Ga_4)O_{12}$:0.1%Pr is the Δ_3 parameter that minimizes the relative error. We notice that the thermometers presenting the lower temperature uncertainty in a broader range also present the median of the relative error distribution at lower values. This is the case, for instance, of $Y_3(Al_3Ga_2)O_{12}$:0.1%Pr, presenting for Δ_1 δT<0.1 K for *ca.* 50 K < T < 600 K (**Figure 6**) and the median of the relative errors below

1%. The conclusion is the same using the decay curves of $Y_3(Al_4Ga_1)O_{12}$:0.1%Pr for which δT<0.1 K for *ca.* 250 K < *T* < 600 K (**Figure 7**) and the median of the relative error is below 0.5%.

Discussion and conclusions

At first, we wish to comment on the composition of the phosphors investigated here in terms of the Pr activator concentration. We deliberately used the 0.1 mol% with respect to Y. As is known from the literature, the $^3P_0$ and $^1D_2$ Pr^{3+} emitting levels experience a non-radiative cross-relaxation for intermediate and high concentrations, as Pr^{3+} 4f→4f luminescence is quite susceptible to concentration quenching [65]. Thus, an increase of the dopant concentration would additionally complicate the interplay between the radiative and non-radiative processes in the phosphors, so important in thermometry as we have seen. While we would not expect any stronger changes in the thermometric parameters for yet lower Pr concentrations, it is obvious that the performance of the investigated garnet thermometers has to change if the Pr content increases. One might claim that, at least in specific ranges of temperature, the sensitivity might increase. Clearly, Pr concentration may be reasonably seen as a parameter useful to master the thermometers' performance and quality. Such experiments, definitely interesting and valuable, would be excessive in this paper.

The change of bandgap is not the only important effect of variation of the Ga:Al ratio in the investigated garnets (as well as other types of phosphors exploiting the bandgap engineering). Continuous replacing of Al with Ga appears also to lower the phonon energies from 800 in $Y_3Al_5O_{12}$ to 700 cm^{-1} in $Y_3Ga_5O_{12}$. This difference is enough to soundly influence the effectiveness of the non-radiative flow of the excited electron from $^3P_0$ to $^1D_2$ level. Accordingly, in the Ga-rich phosphors, the $^3P_0$ emission intensity surpasses the $^1D_2$ luminescence, while in the Al-rich ones the opposite is true. All these effects are seen in **Figures 3, S3, and S7**. Consequently, the change of phonon energies has also a pronounced effect on the intensity ratio of the luminescence bands of interest and, in turn, on the specification of these $Y_3(Al,Ga)_5O_{12}$:0.1%Pr thermometers.

In the investigated garnets, the 4f→5d$_1$ absorption transition appears at relatively long wavelengths, around 270–290 nm, making the excitation of Pr^{3+} luminescence very efficient with standard sources. In many other oxides, not to mention fluorides, this transition is located below 250 nm where excitation with Xe lamp is far less productive. It is also very beneficial that the excitation is executed by a fully allowed 4f→5d transition giving a broad intense absorption band. This makes it possible to record high-quality luminescence spectra with a very high signal-to-noise ratio which results in very low values of uncertainties of temperature measuring. Furthermore, we prove that also in these garnets exploitation of the inter-configurational 5d→4f luminescence of Pr^{3+} ion is very advantageous for the relative sensitivity of the thermometers. Using the intensity ratio of this luminescence and the $^1D_2$ emission, a maximum relative sensitivity S_m = 3.6 %·K^{-1} at 237 K in $Y_3(Al_{1.5}Ga_{3.5})O_{12}$:0.1%Pr and at 60 K in $Y_3(Al_1Ga_4)O_{12}$:0.1%Pr were obtained. It is also noteworthy that the operating range of $Y_3(Al_4Ga_1)O_{12}$:0.1%Pr, whose maximal relative sensitivity reaches the reasonable S_m= 2.9 %·K^{-1} at 261 K, spans the impressive 34–600 K range of temperatures. These are notable results, especially that they should be seen against the background of low-temperature uncertainty, δT, over very broad ranges and even at high temperatures (see **Figure 6b**). These appreciated parameters place the $Y_3(Al,Ga)_5O_{12}$:0.1%Pr garnets within the best thermometers utilizing Pr^{3+} luminescence (see **Table 1** in [23]).

The Ga:Al ratio also strongly affects the decay time of the 5d→4f luminescence, especially the range of temperatures within which its value is temperature-dependent. This can also be successfully utilized for thermometry, see **Figure 4 and 7**. The attained relative maximal sensitivities had reasonable values (0.7–1.5 %·K^{-1}) which were, however, lower than in the case of utilization of the luminescence intensity ratio (**Figure 5 and 6**). Let us note that mostly temperature dependence of the decay times is employed for thermometry at moderate and higher temperatures [3]. Our $Y_3(Al_1Ga_4)O_{12}$:0.1%Pr is an exception permitting the measurement of the temperature through decay time in cryo-region retaining extremally low uncertainty, see **Figure 7**. This becomes possible also due to the bandgap engineering over the whole range of Ga:Al ratio.

Utilization of the two 4f→4f emissions from $^3P_0$ and $^1D_2$ levels (**Figure S10**) was also successfully exploited for temperature measuring broadening in some cases the achievable operating range. In the case of $Y_3Al_5O_{12}$:0.1%Pr it allowed to measure temperature from 17 to 600 K and using $Y_3(Al_{2.5}Ga_{2.5})O_{12}$:0.1%Pr or $Y_3(Al_4Ga_1)O_{12}$:0.1%Pr the range was further enlarged to 17-700 K. Altogether, the use of *both* the 5d→4f and 4f→4f emissions of Pr^{3+} brings important benefits and improves the quality of temperature measurement by such thermometers. A combination of the luminescence intensity ratio and the decay time-temperature dependence further enhances their potential.

Our research confirms that efficient excitation of the luminescence center, taking advantage of allowed transitions, is greatly beneficial and should be considered when designing luminescence thermometers. Suitably positioned allowed transitions ought to be preferred as this improves the quality of temperature measuring. Broad operating range, good relative thermal sensitivity, and low uncertainty are then achievable. What is more, Pr^{3+} offers a few emissions of different temperature characteristics both in terms of their intensities and decay times, which opens the door to dual-mode thermometry. We have proved that thoughtful changes of the phosphors' composition allow for a deliberate management of such important thermometric parameters as (i) operating range, (ii) maximal sensitivity, (iii) range of temperatures of highest thermal sensitivity, and (iv) measurement uncertainty. For each sample, the temperature readout of the distinct thermometric parameters is compared and the statistical analysis of the relative error between the calculated and the measured temperatures emphasizes the impact that the effective temperature readout has on the performance of the thermometers, besides the relative thermal sensitivity and temperature uncertainty. On the other hand, the design of the luminescence thermometers is not easy because the characteristics of the transitions of interest are affected by numerous parameters sensitive to the mentioned compositional variations. As we showed in the present research, managing the bandgap we *simultaneously* affected the phonon energies as well as the phosphor refractive index. Each of them affects the emitting center properties, sometimes in a profound and not always easily predictable way.

This paper proves important advantages the use of the 5d→4f Pr^{3+} luminescence may offer utilizing the luminescence intensity ratio. Yet, also temperature dependence of this emission decay time was found very useful to measure temperature with good sensitivity, low inaccuracy, and – quite surprisingly – over a broad range of temperatures. For $Y_3Al_5O_{12}$:0.1%Pr it is 150-600 K. This makes the $Y_3(Al,Ga)_5O_{12}$:0.1%Pr family of garnets attractive dual-mode luminescence thermometers offering measurements over wide and tunable temperature ranges.

One may wonder if similar results as reported here might be expected in the nanoscale regime. In our opinion, assuming (i) the size of the grains does not fall below, say, 50 nm (to avoid real quantum-size effects) and (ii) the quality of the phosphors is high (lack of OH or other high-energy-phonons impurities), one might expect quite similar performance. Below 5-10 nm, when quantum effects may start playing a role and when the surface-to-volume ratio becomes significant, some changes, even significant, might occur. Consequently, as long as the sizes are not extremally small, measurements on larger crystallites are expected to give reasonable information also on the possible performance of nano-sized counterparts.

Acknowledgements

This research was supported by the Polish National Science Centre (NCN) under grants #UMO2017/25/B/ST5/00824 and 2018/29/B/ST5/00420. This work was also developed within the scope of the project CICECO – Aveiro Institute of Materials, UIDB/50011/2020, financed by Portuguese funds through the FCT/MEC and when appropriate co-financed by FEDER under the PT2020 Partnership Agreement. The financial support from the project NanoHeatControl, POCI-01-0145-FEDER-031469, funded by FEDER, through POCI and by Portuguese funds (OE), through FCT/MCTES, and by European Union's Horizon 2020 FET Open program under grant agreements no. 801305 are acknowledged. E. Z. and L. D. C. are grateful to the Polish National Agency for Academic Exchange (NAWA) for support under the NAWA-Bekker #PPN/BEK/2018/1/00333/DEC/1 and NAWA-Ulam #PPN/

ULM/2019/1/00077/U/00001 projects, respectively. Finally, the authors express their gratitude to referee #4 of our manuscript for the constructive, detailed, didactic, and extremely useful comments that definitively contributed to the improvement of the text.

Figures

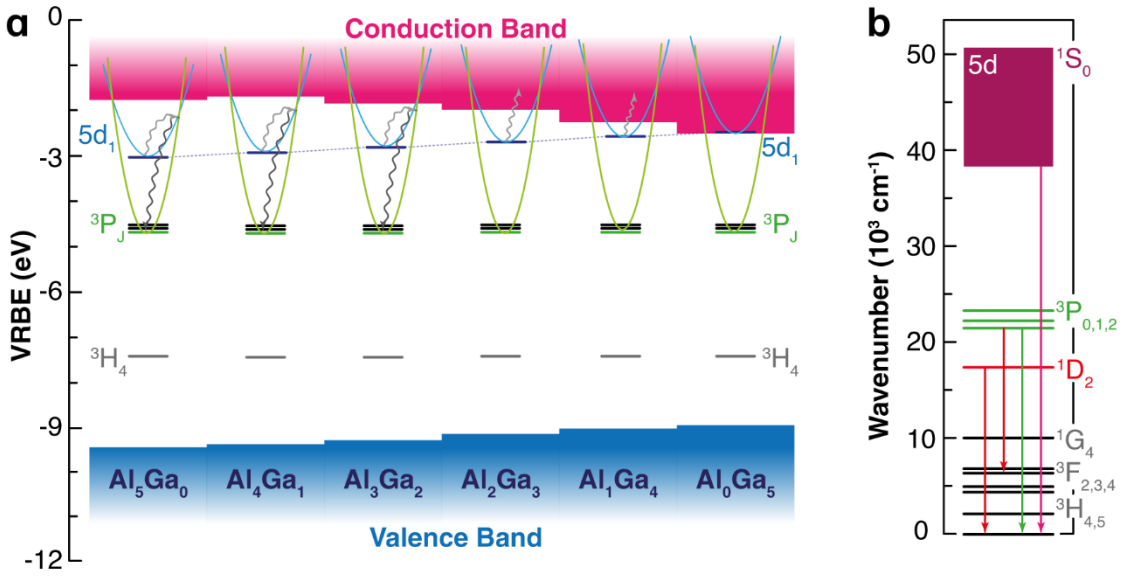

Figure 1. (a) Scheme of bandgap modification in $Y_3(Al,Ga)_5O_{12}$. **(b)** Electronic levels of the Pr^{3+} ion in the $Y_3(Al,Ga)_5O_{12}$ phosphors signaling some specific transitions.

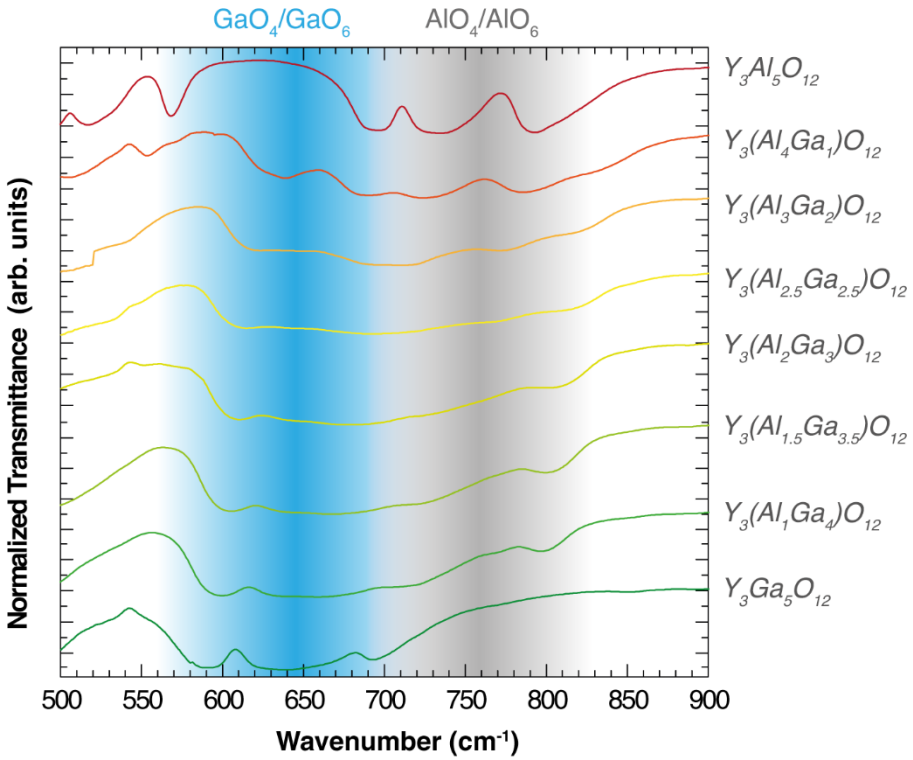

Figure 2. IR spectra of the $Y_3(Al,Ga)_5O_{12}$:0.1%Pr powders in the range of stretching vibrations of Al-O, Ga-O at 300 K.

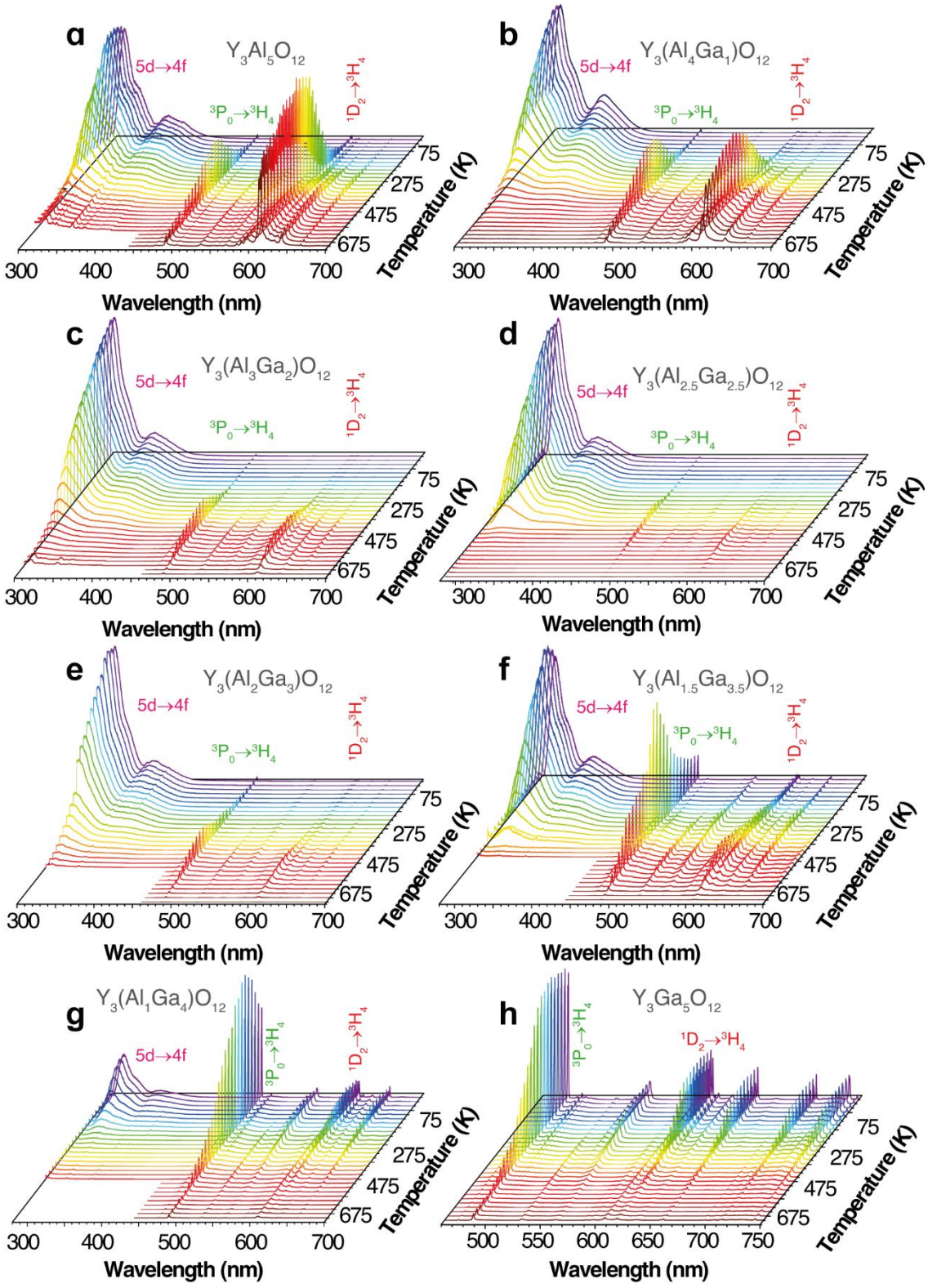

Figure 3. Temperature dependence of the Pr^{3+} luminescence upon 280 nm excitation in the range 17-700 K for $Y_3(Al,Ga)_5O_{12}$:0.1%Pr.

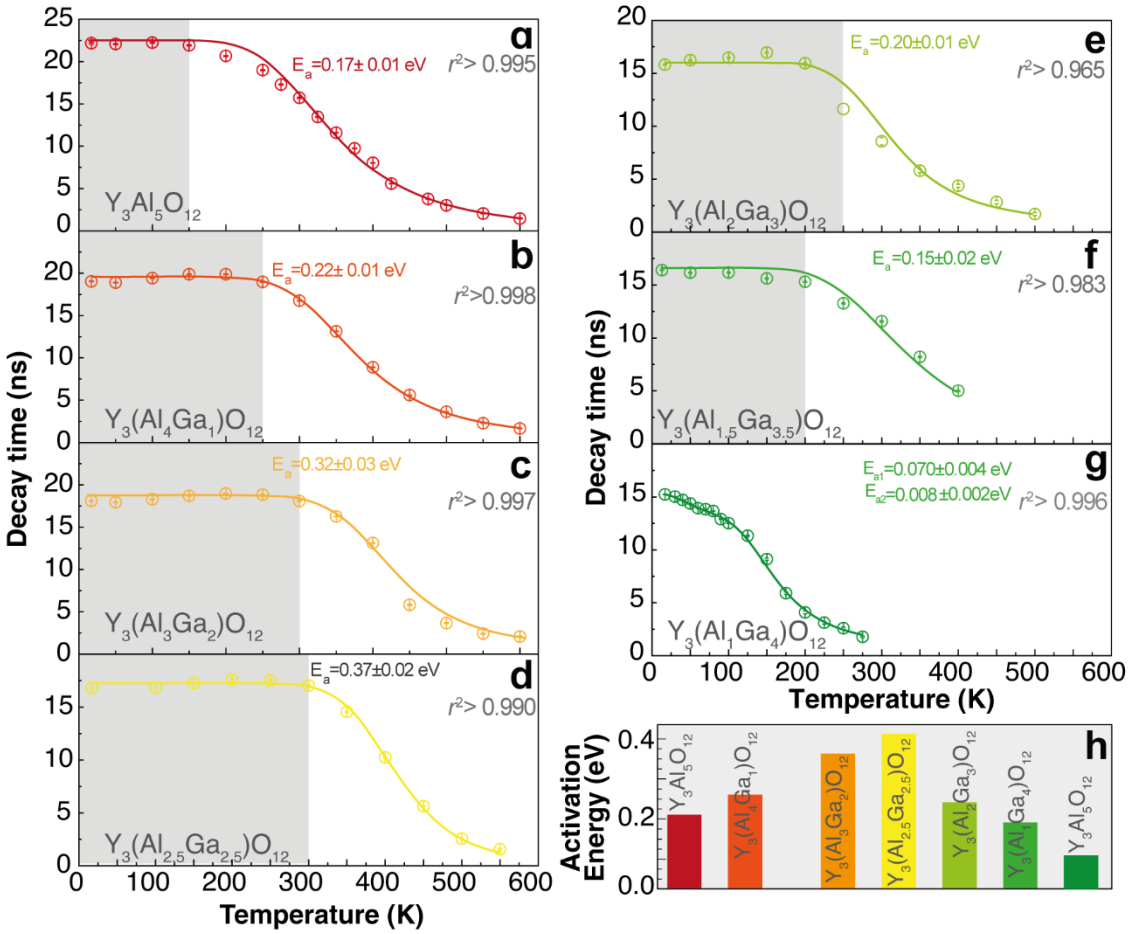

Figure 4. (a-g) Temperature dependence of the 5d→4f Pr^{3+} luminescence decay time in the $Y_3(Al,Ga)_5O_{12}$:0.1%Pr series. Decay traces were measured under 280 nm excitation and luminescence was monitored at 308 nm. Solid lines represent the fits to the experimental data using **Eq. 9** with a single- (a-f) or a double-barrier (g). **(h)** Activation energies derived from the fits as a function of the Ga content. The gray areas represent the limits in which the thermometers are out of their operating ranges.

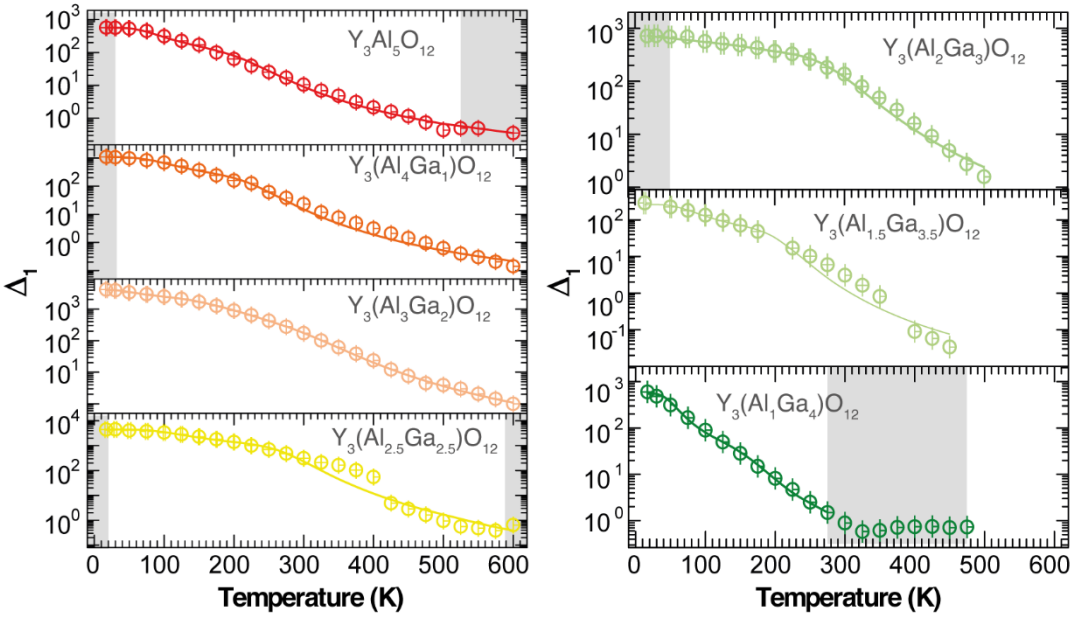

Figure 5. Calibration curves of the $Y_3(Al,Ga)_5O_{12}$:0.1%Pr phosphors using Δ_1. Solid lines represent the fits to the experimental data using the Mott-Seitz model (**Eq. (11)**). The gray areas represent the limits in which the thermometers are out of their operating ranges.

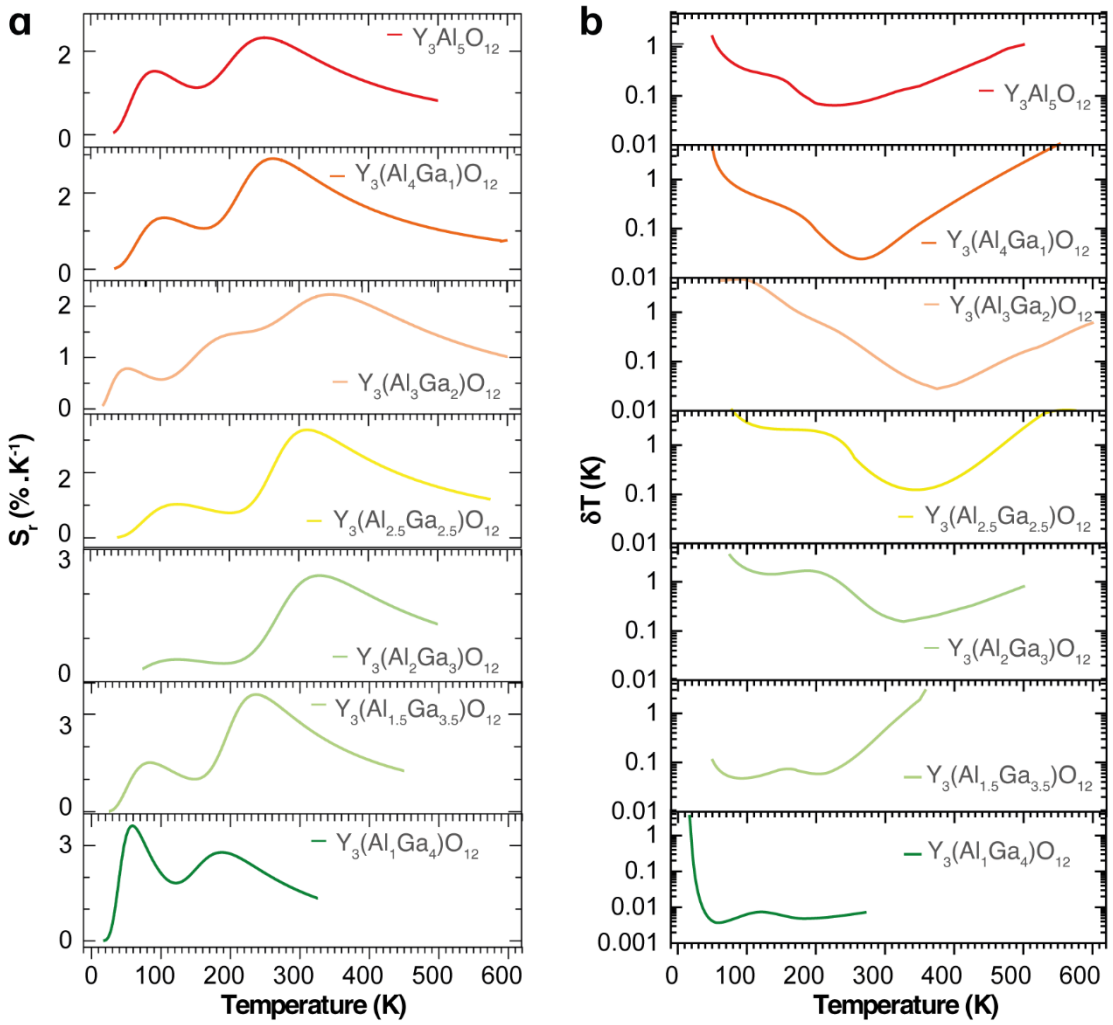

Figure 6. Temperature dependence of the **(a)** relative sensitivity and **(b)** temperature uncertainty for the $Y_3(Al,Ga)_5O_{12}$:0.1%Pr materials using Δ_1.

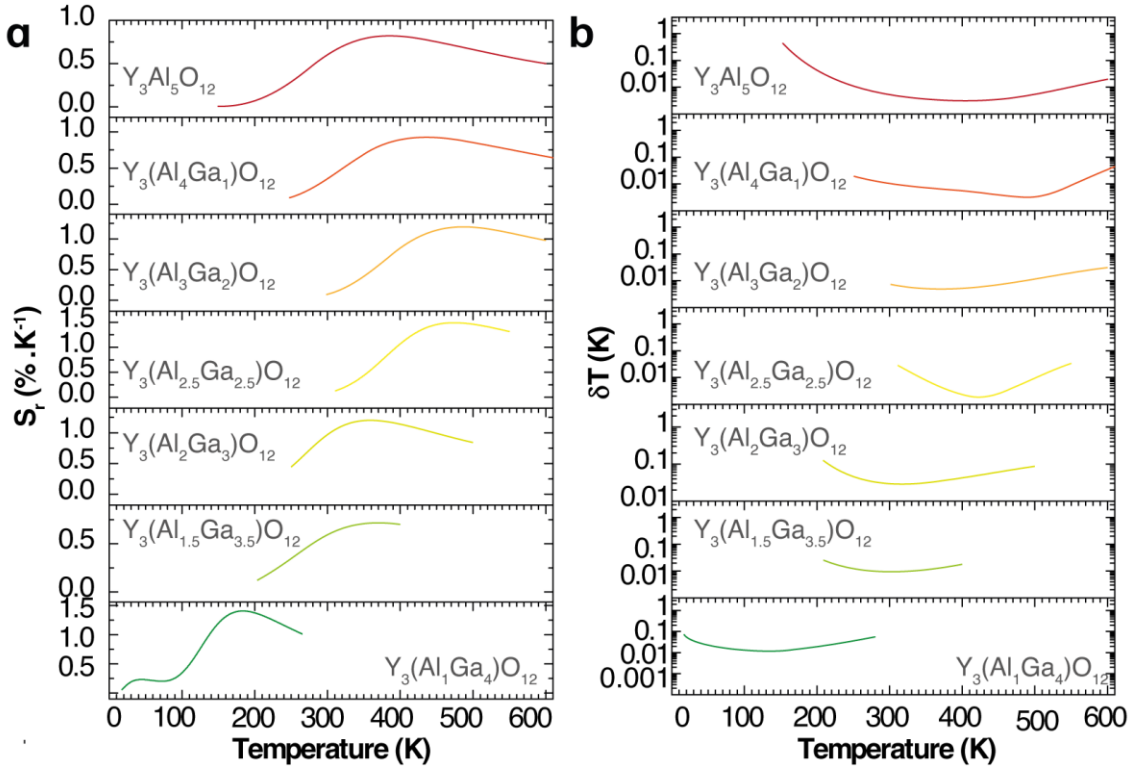

Figure 7. (a) Relative thermal sensitivity and **(b)** temperature uncertainty for all investigated garnets using the decay times of the 5d→4f luminescence as the thermometric parameter.

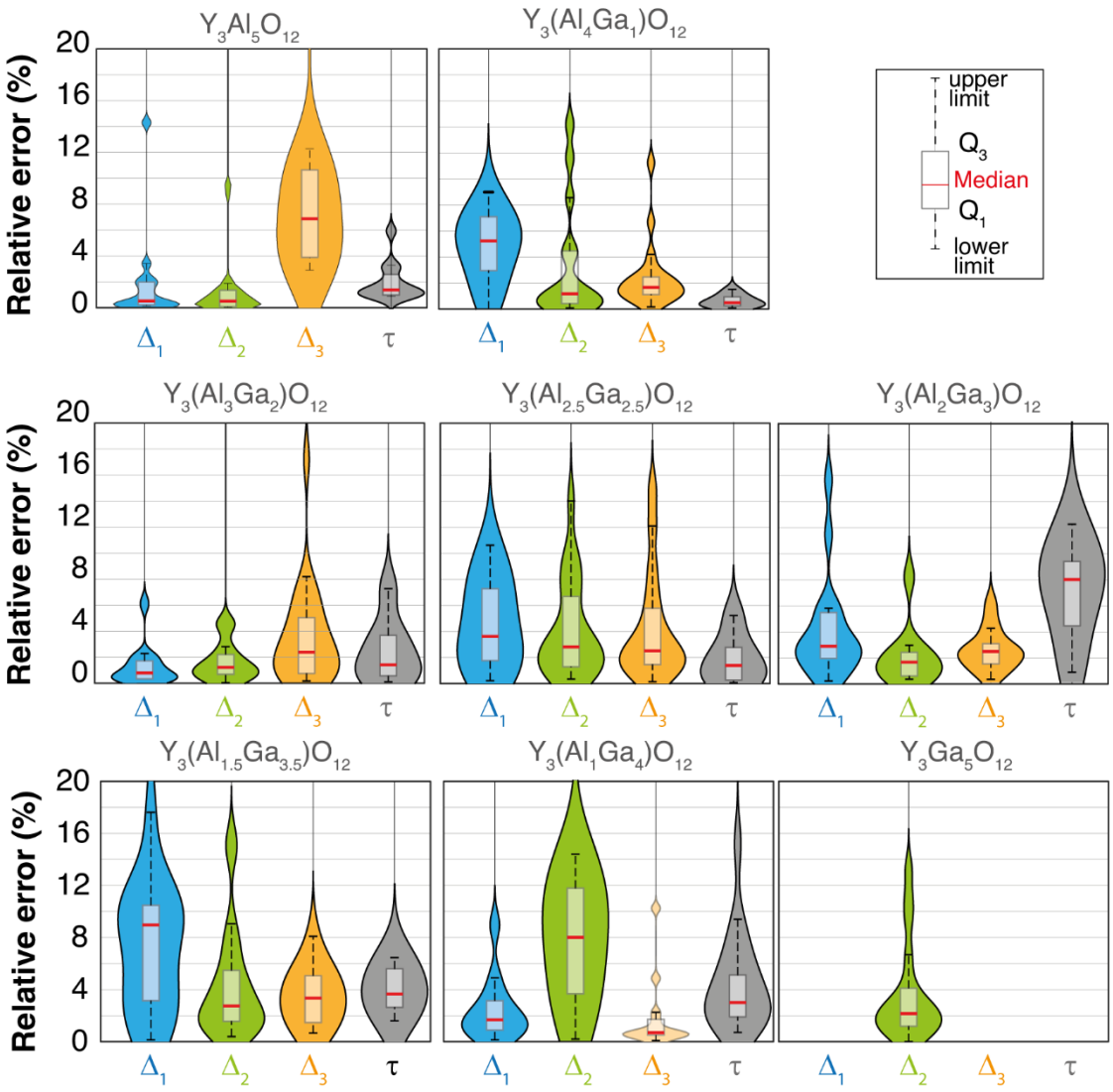

Figure 8. Violin plots of the relative error at the temperature using the distinct thermometric parameters ($\Delta_{1\text{-}3}$ and τ) of all the garnets. The inset shows the boxplot and the corresponding quartiles (Q_1, Q_3), the median, and the lower and higher limits.

Tables

Table 1. Maximum relative thermal sensitivity (S_m), corresponding temperature (T_m), and operating temperature range (ΔT) calculated for Δ_1, Δ_2 and τ in the $Y_3(Al,Ga)_5O_{12}$:0.1%Pr luminescent thermometers. The Ga content is denoted by x.

	Δ_1			Δ_2			τ		
x	S_m (%·K^{-1})	T_m (K)	ΔT (K)	S_m (%·K^{-1})	T_m (K)	ΔT (K)	S_m (%·K^{-1})	T_m (K)	ΔT (K)
0.0	2.4	250	33–500	2.5	600	17–600	0.8	378	150-600
1.0	2.9	261	34–600	0.6	700	17–700	1.0	430	250-600
2.0	2.3	345	17–600	0.6	700	290–700	1.2	480	300-600
2.5	3.1	340	30–575	0.6	420	17–700	1.5	480	310-550
3.0	2.5	327	75–500	1.0	100	80–280	1.2	360	250-500
				0.4	600	330–600			
3.5	3.6	237	25–450	1.0	480	13–580	0.7	350	200-400
4.0	3.6	60	17–275	0.3	520	17–580	1.4	184	15-275
5.0	---	---	---	0.9	405	125–550	---	---	---

References

[1] C.D.S. Brites, A. Millán, L.D. Carlos, Lanthanides in Luminescent Thermometry, Handbook on the Physics and Chemistry Of Rare Earths, 49 (2016) 339–427.

[2] R. Piñol, C.D.S. Brites, N.J. Silva, L.D. Carlos, A. Millán, Nanoscale Thermometry for Hyperthermia Applications, in: Nanomater. Magn. Opt. Hyperth. Appl., Elsevier, 2019: pp. 139–172. doi:10.1016/B978-0-12-813928-8.00006-5.

[3] M.D. Dramićanin, Luminescence Thermometry Methods, Materials, and Applications, Woodhead Publishing, 2018.

[4] D. Jaque, F. Vetrone, Luminescence nanothermometry, Nanoscale. 4 (2012) 4301. doi:10.1039/c2nr30764b.

[5] J. Zhong, D. Chen, Y. Peng, Y. Lu, X. Chen, X. Li, Z. Ji, A review on nanostructured glass ceramics for promising application in optical thermometry, J. Alloys Compd. 763 (2018) 34–48. doi:10.1016/j.jallcom.2018.05.348.

[6] M. Back, J. Ueda, M.G. Brik, T. Lesniewski, M. Grinberg, S. Tanabe, Revisiting Cr^{3+}-Doped $Bi_2Ga_4O_9$ Spectroscopy: Crystal Field Effect and Optical Thermometric Behavior of Near-Infrared-Emitting Singly-Activated Phosphors, ACS Appl. Mater. Interfaces. 10 (2018) 41512–41524. doi:10.1021/acsami.8b15607.

[7] M. Back, E. Trave, J. Ueda, S. Tanabe, Ratiometric optical thermometer based on dual near-infrared emission in Cr^{3+}-doped bismuth-based gallate host, Chem. Mater. 28 (2016) 8347–8356.

[8] J. Drabik, B. Cichy, L. Marciniak, New Type of Nanocrystalline Luminescent Thermometers Based on Ti^{3+}/Ti^{4+} and Ti^{4+}/Ln^{3+} (Ln^{3+}=Nd^{3+}, Eu^{3+}, Dy^{3+}) Luminescence Intensity Ratio, J. Phys. Chem. C. 122 (2018) 14928–14936. doi:10.1021/acs.jpcc.8b02328.

[9] E. Carrasco, B. del Rosal, F. Sanz-Rodríguez, Á.J. de la Fuente, P.H. Gonzalez, U. Rocha, K.U. Kumar, C. Jacinto, J.G. Solé, D. Jaque, Intratumoral Thermal Reading During Photo-Thermal Therapy by Multifunctional Fluorescent Nanoparticles, Adv. Funct. Mater. 25 (2015) 615–626. doi:10.1002/adfm.201403653.

[10] U. Rocha, C. Jacinto da Silva, W. Ferreira Silva, I. Guedes, A. Benayas, L. Martínez Maestro, M. Acosta Elias, E. Bovero, F.C.J.M. van Veggel, J.A. García Solé, D. Jaque, Subtissue Thermal Sensing Based on Neodymium-Doped LaF_3 Nanoparticles, ACS Nano. 7 (2013) 1188–1199. doi:10.1021/nn304373q.

[11] A. Benayas, B. del Rosal, A. Pérez-Delgado, K. Santacruz-Gómez, D. Jaque, G.A. Hirata, F. Vetrone, Nd:YAG Near-Infrared Luminescent Nanothermometers, Adv. Opt. Mater. 3 (2015) 687–694. doi:10.1002/adom.201400484.

[12] M.R. Cates, D.L. Beshears, S.W. Allison, C.M. Simmons, Phosphor thermometry at cryogenic temperatures, Rev. Sci. Instrum. 68 (1997) 2412–2417. doi:10.1063/1.1148125.

[13] B. Zhuang, Y. Liu, S. Yuan, H. Huang, J. Chen, D. Chen, Glass stabilized ultra-stable dual-emitting Mn-doped cesium lead halide perovskite quantum dots for cryogenic temperature sensing, Nanoscale. 11 (2019) 15010–15016. doi:10.1039/C9NR05831A.

[14] M.D. Dramićanin, Trends in luminescence thermometry, J. Appl. Phys. 128 (2020) 040902. doi:10.1063/5.0014825.

[15] S.W. Allison, D.L. Beshears, M.R. Cates, M.B. Scudiere, D.W. Shaw, A.D. Ellis, Luminescence of YAG:Dy and YAG:Dy,Er crystals to 1700 °C, Meas. Sci. Technol. 31 (2020). doi:10.1088/1361-6501/ab4ebd.

[16] M.D. Dramićanin, Sensing temperature via downshifting emissions of lanthanide-doped metal oxides and salts. A review, Methods Appl. Fluoresc. 4 (2016) 042001. doi:10.1088/2050-6120/4/4/042001.

[17] L. Marciniak, K. Trejgis, Luminescence lifetime thermometry with Mn^{3+}–Mn^{4+} co-doped nanocrystals, J. Mater. Chem. C. 6 (2018) 7092–7100. doi:10.1039/C8TC01981A.

[18] K. Trejgis, L. Marciniak, The influence of manganese concentration on the sensitivity of bandshape

and lifetime luminescent thermometers based on $Y_3Al_5O_{12}$:Mn^{3+}, Mn^{4+}, Nd^{3+} nanocrystals, Phys. Chem. Chem. Phys. 20 (2018) 9574–9581. doi:10.1039/C8CP00558C.

[19] M. Sekulić, Z. Ristić, B. Milićević, Ž. Antić, V. Đorđević, M.D. Dramićanin, $Li_{1.8}Na_{0.2}TiO_3$:Mn^{4+}: The highly sensitive probe for the low-temperature lifetime-based luminescence thermometry, Opt. Commun. 452 (2019) 342–346. doi:10.1016/j.optcom.2019.07.056.

[20] C.D.S. Brites, K. Fiaczyk, J.F.C.B. Ramalho, M. Sójka, L.D. Carlos, E. Zych, Widening the Temperature Range of Luminescent Thermometers through the Intra- and Interconfigurational Transitions of Pr^{3+}, Adv. Opt. Mater. 6 (2018) 1701318. doi:10.1002/adom.201701318.

[21] M. Sójka, J.F.C.B. Ramalho, C.D.S. Brites, K. Fiaczyk, L.D. Carlos, E. Zych, Bandgap Engineering and Excitation Energy Alteration to Manage Luminescence Thermometer Performance. The Case of $Sr_2(Ge,Si)O_4$:Pr^{3+}, Adv. Opt. Mater. 7 (2019) 1901102. doi:10.1002/adom.201901102.

[22] S. Wang, S. Ma, G. Zhang, Z. Ye, X. Cheng, High-Performance Pr^{3+} -Doped Scandate Optical Thermometry: 200 K of Sensing Range with Relative Temperature Sensitivity above $2\%\cdot K^{-1}$, ACS Appl. Mater. Interfaces. 11 (2019) 42330–42338. doi:10.1021/acsami.9b13873.

[23] M. Sójka, C. D. S. Brites, L. A. D. Carlos and E. Zych, J. Mater. Chem. C, 2020, DOI: 10.1039/D0TC01958E, (n.d.).

[24] J. Ueda, A. Meijerink, P. Dorenbos, A.J.J. Bos, S. Tanabe, Thermal ionization and thermally activated crossover quenching processes for 5d-4f luminescence in $Y_3Al_{5-x}Ga_xO_{12}$:Pr^{3+}, Phys. Rev. B. 95 (2017) 014303. doi:10.1103/PhysRevB.95.014303.

[25] Z. Xia, A. Meijerink, Ce^{3+} -Doped garnet phosphors: composition modification, luminescence properties and applications, Chem. Soc. Rev. 46 (2017) 275–299. doi:10.1039/C6CS00551A.

[26] T. Zorenko, V. Gorbenko, S. Nizankovskiy, Y. Zorenko, Comparison of the Luminescent Properties of $Y_3Al_5O_{12}$:Pr Crystals and Films, Acta Phys. Pol. A. 133 (2018) 948–953. doi:10.12693/APhysPolA.133.948.

[27] Y. Tang, S. Zhou, X. Yi, D. Hao, X. Shao, J. Chen, The characterization of Ce/Pr-doped YAG phosphor ceramic for the white LEDs, J. Alloys Compd. 745 (2018) 84–89. doi:10.1016/j.jallcom.2018.02.129.

[28] J. Ueda, P. Dorenbos, A.J.J. Bos, K. Kuroishi, S. Tanabe, Control of electron transfer between Ce^{3+} and Cr^{3+} in the $Y_3Al_{5-x}Ga_xO_{12}$ host via conduction band engineering, J. Mater. Chem. C. 3 (2015) 5642–5651. doi:10.1039/C5TC00546A.

[29] M. Fasoli, A. Vedda, M. Nikl, C. Jiang, B.P. Uberuaga, D.A. Andersson, K.J. McClellan, C.R. Stanek, Band-gap engineering for removing shallow traps in rare-earth $Lu_3Al_5O_{12}$ garnet scintillators using Ga^{3+} doping, Phys. Rev. B - Condens. Matter Mater. Phys. 84 (2011) 1–4.

[30] A.J.J. Bos, Thermoluminescence as a research tool to investigate luminescence mechanisms, Materials (Basel). 10 (2017) 1–22.

[31] J. Luo, Y. Wu, G. Zhang, H. Zhang, G. Ren, Composition–property relationships in $(Gd_{3-x}Lu_x)(Ga_yAl_{5-y})O_{12}$:Ce (x=0, 1, 2, 3 and y=0, 1, 2, 3, 4) multicomponent garnet scintillators, Opt. Mater. (Amst). 36 (2013) 476–481. doi:10.1016/j.optmat.2013.10.012.

[32] Y. Katayama, A. Hashimoto, J. Xu, J. Ueda, S. Tanabe, Thermoluminescence investigation on $Y_3Al_{5-x}Ga_xO_{12}$:Ce^{3+}-Bi^{3+} green persistent phosphors, J. Lumin. 183 (2017) 355–359. doi:10.1016/j.jlumin.2016.11.074.

[33] P. Dorenbos, Electronic structure and optical properties of the lanthanide activated $RE_3(Al_{1-x}Ga_x)_5O_{12}$ (RE=Gd, Y, Lu) garnet compounds, J. Lumin. 134 (2013) 310–318. doi:10.1016/j.jlumin.2012.08.028.

[34] C.D.S. Brites, S. Balabhadra, L.D. Carlos, Lanthanide-Based Thermometers: At the Cutting-Edge of Luminescence Thermometry, Adv. Opt. Mater. 7 (2019) 1801239. doi:10.1002/adom.201801239.

[35] G. Blasse, B.C. Grabmaier, Luminescent Materials, Springer-Verlag, Berlin Heidelberg, 1994.

[36] J. Mooney, P. Kambhampati, Get the Basics Right: Jacobian Conversion of Wavelength and Energy Scales for Quantitative Analysis of Emission Spectra, J. Phys. Chem. Lett. 4 (2013) 3316–3318. doi:10.1021/jz401508t.

[37] M. Suta, A. Meijerink, A Theoretical Framework for Ratiometric Single Ion Luminescent Thermometers—Thermodynamic and Kinetic Guidelines for Optimized Performance, Adv. Theory Simulations. 3 (2020) 2000176. doi:10.1002/adts.202000176.
[38] C.D.S. Brites, P.P. Lima, N.J.O. Silva, A. Millan, F. Palacio, V.S. Amaral, L.D. Carlos, Nanoscale Thermometry at the nanoscale, Nanoscale. 4 (2012) 4799–4829. doi:10.1039/c2nr30663h.
[39] M. Jia, Z. Sun, M. Zhang, H. Xu, Z. Fu, What determines the performance of lanthanide-based ratiometric nanothermometers?, Nanoscale. 12 (2020) 20776–20785.
[40] A. Bednarkiewicz, L. Marciniak, L.D. Carlos, D. Jaque, Standardizing luminescence nanothermometry for biomedical applications, Nanoscale. 12 (2020) 14405–14421. doi:10.1039/D0NR03568H.
[41] S. Kostić, Z.Ž. Lazarević, V. Radojević, A. Milutinović, M. Romčević, N.Ž. Romčević, A. Valčić, Study of structural and optical properties of YAG and Nd:YAG single crystals, Mater. Res. Bull. 63 (2015) 80–87. doi:10.1016/j.materresbull.2014.11.033.
[42] Ł. Dobrzycki, E. Bulska, D.A. Pawlak, Z. Frukacz, K. Woźniak, Structure of YAG Crystals Doped/Substituted with Erbium and Ytterbium, Inorg. Chem. 43 (2004) 7656–7664. doi:10.1021/ic049920z.
[43] R.D. Shannon, Revised effective ionic radii and systematic studies of interatomic distances in halides and chalcogenides, Acta Crystallogr. Sect. A. 32 (1976) 751–767.
[44] P. Sengar, H.A. Borbón-Nuñez, C.J. Salas-Juárez, E.M. Aguilar, C. Cruz-Vázquez, R. Bernal, G.. Hirata, β-Irradiated thermoluminescence response of nanocrystalline YAGG:Pr^{3+} for radiation dosimetry, Mater. Res. Bull. 90 (2017) 195–204. doi:10.1016/j.materresbull.2017.03.001.
[45] H.S. Yoder, M.L. Keith, Complete Substitution of Aluminum for Silicon - the System $3MnO{\cdot}Al_2O_3{\cdot}3SiO_2$-$3Y_2O_{3.5}Al_2O_3$, Geol. Soc. Am. Bull. 61 (1950) p1516–p1517.
[46] P. Fischer, W. Hälg, E. Stoll, A. Segmüller, X-ray and neutron diffraction study of the substitutional disorder in the yttrium-iron-gallium garnets, Acta Crystallogr. 21 (1966) 765–769. doi:10.1107/S0365110X66003827.
[47] Y.-C. Lin, M. Karlsson, M. Bettinelli, Inorganic Phosphor Materials for Lighting, Top. Curr. Chem. 374 (2016) 21. doi:10.1007/s41061-016-0023-5.
[48] K. Papagelis, S. Ves, Vibrational properties of the rare earth aluminum garnets, J. Appl. Phys. 94 (2003) 6491–6498. doi:10.1063/1.1623328.
[49] Y.C. Lin, M. Karlsson, M. Bettinelli, Inorganic phosphor materials for lighting, Top. Curr. Chem. 374 (2016) 374–421. doi:10.1007/s41061-016-0023-5.
[50] J. Ueda, K. Aishima, S. Tanabe, Temperature and compositional dependence of optical and optoelectronic properties in Ce^{3+}-doped $Y_3Sc_2Al_{3-x}Ga_xO_{12}$(x = 0, 1, 2, 3), Opt. Mater. (Amst). 35 (2013) 1952–1957.
[51] J. Ueda, P. Dorenbos, A.J.J. Bos, A. Meijerink, S. Tanabe, Insight into the Thermal Quenching Mechanism for $Y_3Al_5O_{12}$:Ce^{3+} through Thermoluminescence Excitation Spectroscopy, J. Phys. Chem. C. 119 (2015) 25003–25008. doi:10.1021/acs.jpcc.5b08828.
[52] G.H. Dieke, H. Crosswhite, Spectra and energy levels of rare earth ions in crystals, Interscience Publishers Wiley, New York, 1968.
[53] K. Fiaczyk, S. Omagari, A. Meijerink, E. Zych, Temperature dependence of $4f^{n-1}5d^1 \rightarrow 4f^n$ luminescence of Ce^{3+} and Pr^{3+} ions in Sr_2GeO_4 host, J. Lumin. 198 (2018) 163–170.
[54] J. Pejchal, M. Nikl, E. Mihóková, J.A. Mareš, A. Yoshikawa, H. Ogino, K.M. Schillemat, A. Krasnikov, A. Vedda, K. Nejezchleb, V. Múčka, Pr^{3+} -doped complex oxide single crystal scintillators, J. Phys. D. Appl. Phys. 42 (2009) 055117. doi:10.1088/0022-3727/42/5/055117.
[55] C.W.E. van Eijk, P. Dorenbos, R. Visser, Nd^{3+} and Pr^{3+} doped inorganic scintillators, IEEE Trans. Nucl. Sci. 41 (1994) 738–741. doi:10.1109/23.322798.
[56] A. Zych, M. De Lange, C. De Mello Donegá, A. Meijerink, Analysis of the radiative lifetime of Pr^{3+} d-f emission, J. Appl. Phys. 112 (2012) 013536-1–2.
[57] B. Henderson, G.. Imbusch, Optical Spectroscopy of Inorganic Solids, Clarendon Pres-Oxford,

Oxford, 1989.
[58] M.S. Pudovkin, O.A. Morozov, V. V. Pavlov, S.L. Korableva, E. V. Lukinova, Y.N. Osin, V.G. Evtugyn, R.A. Safiullin, V. V. Semashko, Physical Background for Luminescence Thermometry Sensors Based on Pr^{3+}:LaF_3 Crystalline Particles, J. Nanomater. 2017 (2017) 1–9. doi:10.1155/2017/3108586.
[59] N.F. Mott, On the absorption of light by crystals, Proc. R. Soc. LONDON Ser. A. 167 (1938) 384.
[60] D. Ananias, F.A.A. Paz, D.S. Yufit, L.D. Carlos, J. Rocha, Photoluminescent Thermometer Based on a Phase-Transition Lanthanide Silicate with Unusual Structural Disorder, J. Am. Chem. Soc. 137 (2015) 3051–3058. doi:10.1021/ja512745y.
[61] E. Zych, C. Brecher, J. Glodo, Kinetics of cerium emission in a YAG:Ce single crystal: the role of traps temperatures, J. Condend. Matter. 12 (2000) 1947–1958.
[62] M. Nikl, J. Pejchal, E. Mihóková, J.A. Mares, H. Ogino, A. Yoshikawa, T. Fukuda, A. Vedda, C. D'Ambrosio, Antisite defect-free $Lu_3(Ga_xAl_{1-x})_5O_{12}$:Pr scintillator, Appl. Phys. Lett. 88 (2006) 1–2. doi:10.1063/1.2191741.
[63] H. Ogino, A. Yoshikawa, M. Nikl, J. Pejchal, T. Fukuda, Growth and Luminescence Properties of Pr-doped $Lu_3(Ga,Al)_5O_{12}$ Single Crystals, Jpn. J. Appl. Phys. 46 (2007) 3514–3517.
[64] R.G. Geitenbeek, H.W. de Wijn, A. Meijerink, Non-Boltzmann Luminescence in $NaYF_4$:Eu^{3+}: Implications for Luminescence Thermometry, Phys. Rev. Appl. 10 (2018) 064006. doi:10.1103/PhysRevApplied.10.064006.
[65] J. Collins, M. Geen, M. Bettinelli, B. Di Bartolo, Dependence of cross-relaxation on temperature and concentration from the $^1D_2$ level of Pr^{3+} in YPO_4, J. Lumin. 132 (2012) 2626–2633. doi:10.1016/j.jlumin.2012.04.027.